Metal dependence and branched RNA cocrystal structures of the RNA lariat debranching enzyme Dbr1

Nathaniel E. Clark[a,1,2], Adam Katolik[b,1], Kenneth M. Roberts[c], Alexander B. Taylor[a,d], Stephen P. Holloway[a], Jonathan P. Schuermann[e], Eric J. Montemayor[f], Scott W. Stevens[g,h], Paul F. Fitzpatrick[a,2], Masad J. Damha[b,2], and P. John Hart[a,d,i,2]

[a]Department of Biochemistry and Structural Biology, University of Texas Health Science Center, San Antonio, TX 78229; [b]Department of Chemistry, McGill University, Montreal, QC H3A 0B8, Canada; [c]Department of Chemistry & Physics, University of South Carolina Aiken, Aiken, SC 29811; [d]X-ray Crystallography Core Laboratory, University of Texas Health Science Center, San Antonio, TX 78229; [e]Northeastern Collaborative Access Team, Department of Chemistry and Chemical Biology, Cornell University, Ithaca, NY 14853; [f]Departments of Biochemistry and Biomolecular Chemistry, University of Wisconsin, Madison, WI 53706; [g]Department of Molecular Biosciences, The University of Texas, Austin, TX 78712; [h]Institute for Cellular and Molecular Biology, The University of Texas, Austin, TX 78712; and [i]Department of Veterans Affairs, South Texas Veterans Health Care System, San Antonio, TX 78229.

Edited by Graham C. Walker, Massachusetts Institute of Technology, Cambridge, MA, and approved November 15, 2016 (received for review August 1, 2016)

Intron lariats are circular, branched RNAs (bRNAs) produced during pre-mRNA splicing. Their unusual chemical and topological properties arise from branch-point nucleotides harboring vicinal 2′,5′- and 3′,5′-phosphodiester linkages. The 2′,5′-bonds must be hydrolyzed by the RNA debranching enzyme Dbr1 before spliced introns can be degraded or processed into small nucleolar RNA and microRNA derived from intronic RNA. Here, we measure the activity of Dbr1 from *Entamoeba histolytica* by using a synthetic, dark-quenched bRNA substrate that fluoresces upon hydrolysis. Purified enzyme contains nearly stoichiometric equivalents of Fe and Zn per polypeptide and demonstrates turnover rates of ∼3 s^{-1}. Similar rates are observed when apo-Dbr1 is reconstituted with Fe(II)+Zn(II) under aerobic conditions. Under anaerobic conditions, a rate of ∼4.0 s^{-1} is observed when apoenzyme is reconstituted with Fe(II). In contrast, apo-Dbr1 reconstituted with Mn(II) or Fe(II) under aerobic conditions is inactive. Diffraction data from crystals of purified enzyme using X-rays tuned to the Fe absorption edge show Fe partitions primarily to the β-pocket and Zn to the α-pocket. Structures of the catalytic mutant H91A in complex with 7-mer and 16-mer synthetic bRNAs reveal bona fide RNA branchpoints in the Dbr1 active site. A bridging hydroxide is in optimal position for nucleophilic attack of the scissile phosphate. The results clarify uncertainties regarding structure/function relationships in Dbr1 enzymes, and the fluorogenic probe permits high-throughput screening for inhibitors that may hold promise as treatments for retroviral infections and neurodegenerative disease.

RNA debranching | intron lariat | enzyme kinetics | X-ray crystallography | Dbr1

The enzymatic processing of diverse RNA molecules requires selective recognition of their unique physicochemical properties. The sequential *trans*-esterification reactions catalyzed by the spliceosome yield mature messenger RNA (mRNA) and excised intron lariats (1, 2), the latter of which contain internal branchpoint adenosine nucleotides harboring vicinal 2′,5′- and 3′,5′-phosphodiester linkages (3). Mature mRNA transcripts are exported to the cytosol for protein synthesis, but lariat introns must be linearized before they can be turned over or processed into the subset of small nucleolar RNAs and microRNAs that are derived from intronic RNA (4, 5). The lariat forms when the 2′-hydroxyl group of an adenosine nucleotide near the 3′-end of the intron acts as the nucleophile to attack the 5′-splice site, producing 5′-exon-3′-OH and intron lariat/3′-exon intermediates. The 3′-hydroxyl group of the 5′-exon-3′-OH intermediate subsequently acts as the nucleophile to attack the 3′-splice site, resulting in intron excision and exon ligation (6, 7) (Fig. 1*A*). The resulting vicinal 2′,5′- and 3′,5′-phosphodiester linkages confer unique topological and chemical features to the branchpoint and flanking nucleotides, and these lariats persist in yeast cells lacking active Dbr1 (RNA lariat debranching enzyme) protein (8), the metallophosphoesterase known as the RNA (intron) debranching enzyme. Intron lariats accumulate to unnaturally high levels in Δ*dbr1* strains of *Saccharomyces cerevisiae*, suggesting hydrolysis of the 2′,5′-linkages is rate-limiting in intron processing and turnover after splicing (8). A central role for Dbr1 activity in normal RNA metabolism is supported by findings that Δ*dbr1* strains of *Schizosaccharomyces pombe* exhibit severe morphological and growth defects (9), whereas ablation of the *DBR1* gene in higher eukaryotes is lethal (10, 11), presumably due to their need for a larger array of essential intron-derived small nucleolar RNAs and microRNAs.

RNA debranching activity was first detected in HeLa cell extracts in 1985 (3). Hydrolysis was selective for 2′,5′-phosphodiester linkages, but RNA nucleotides linked solely by 2′,5′-phosphodiester bonds were not substrates, suggesting the vicinal 2′,5′- and 3′,5′-phosphodiester linkages act as specificity determinants in RNA lariat branchpoint recognition (3). The addition of 10 mM EDTA abolished activity, suggesting a requirement for divalent cations (12). The gene encoding the enzyme was subsequently identified in a yeast genetic screen designed to identify factors involved in Ty1 retrotransposon mobility. Ablation of the *DBR1* gene reduced the frequency of transposition with the concomitant accumulation of intron lariats (8). More recently, knockdown of human Dbr1 (hDbr1)

Significance

The RNA lariat debranching enzyme Dbr1 cleaves the 2′,5′-phosphodiester linkages in intron lariats generated during pre-mRNA splicing. The enzyme is central to RNA metabolism because its activity is required for intron turnover and for the production of small nucleolar RNAs and microRNAs encoded in intronic RNA. Here, the kinetics of Dbr1-mediated debranching of a synthetic RNA substrate are measured by using apoenzyme reconstituted with various divalent cations. The results suggest Fe and Zn are preferred cofactors. Structures of a binuclear catalytic mutant in complex with bona fide branched RNAs reveal a metal-bridging hydroxide positioned to attack the scissile phosphate. The results clarify structure/function relationships in Dbr1 enzymes and are guiding the search for inhibitors that hold promise as therapies for retroviral infections and neurodegenerative disease.

Author contributions: N.E.C., A.K., S.W.S., P.F.F., M.J.D., and P.J.H. designed research; N.E.C., A.K., K.M.R., A.B.T., S.P.H., and J.P.S. performed research; N.E.C., A.K., E.J.M., and M.J.D. contributed new reagents/analytic tools; N.E.C., A.K., K.M.R., A.B.T., S.W.S., P.F.F., M.J.D., and P.J.H. analyzed data; and N.E.C., S.W.S., M.J.D., and P.J.H. wrote the paper.

The authors declare no conflict of interest.

This article is a PNAS Direct Submission.

Data deposition: The atomic coordinates and structure factors have been deposited in the Protein Data Bank, www.pdb.org (PDB ID codes 5K71, 5K73, 5K77, and 5K78).

[1]N.E.C. and A.K. contributed equally to this work.

[2]To whom correspondence may be addressed. Email: clarkn@uthscsa.edu, fitzpatrickp@uthscsa.edu, masad.damha@mcgill.ca, or pjh@biochem.uthscsa.edu.

This article contains supporting information online at www.pnas.org/lookup/suppl/doi:10.1073/pnas.1612729114/-/DCSupplemental.

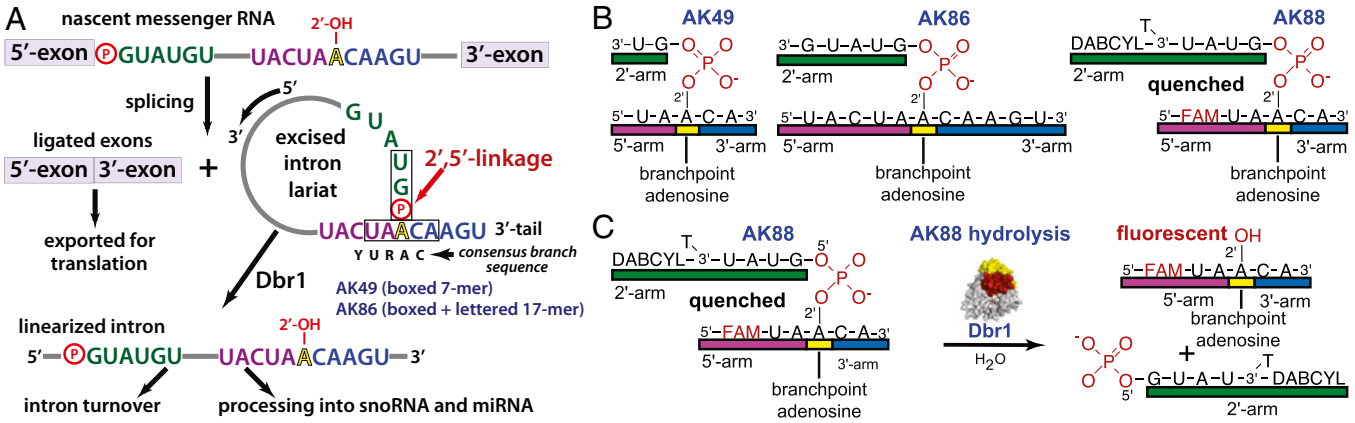

Fig. 1. Dbr1 in pre-mRNA splicing and synthetic bRNAs used in this study. (*A*) The phosphate of the branching 2′,5′-phosphodiester bond is circled in red. The coloring of the branchpoint and flanking nucleotides is preserved throughout the manuscript. The sequence of the synthetic bRNAs AK86 is displayed, and the shorter AK49 sequence is boxed. (*B*) Cartoon representation of AK49, AK86, and AK88. (*C*) Dbr1-mediated hydrolysis of the fluorogenic bRNA AK88 permits the 2′- and 5′-arms to separate, relieving the quenching of the 5′-FAM fluorophore by the 2′-DABCYL moiety.

gene expression was reported to significantly diminish retroviral replication in cells infected with the HIV (13, 14). This observation is consistent with the evolutionarily conserved genetic structures and replication mechanisms of retrotransposons and retroviruses (15, 16). Together, these studies implicate the RNA lariat debranching enzyme as a participant in retroelement and retroviral replication, although the precise mechanism(s) through which it facilitates these processes remains unclear. Hypotheses regarding the molecular mechanism(s) of Dbr1 in these systems are discussed (17–21).

Yeast Dbr1 isolated from *Escherichia coli* was reported to possess biochemical properties indistinguishable from the enzyme isolated from yeast (22). Substrates included Y-like *trans*-splicing intermediates, group II intron lariats, and multicopy single-stranded DNAs (msDNAs) in which the RNA components are attached to the 5′-DNA portions via 2′,5′-phosphodiester linkages (22). Yeast Dbr1 (yDbr1) was active "as-purified," although EDTA inhibited activity at concentrations of 25 mM or greater, reinforcing the suggestion that a bound metal ion is required for debranching activity. Debranching experiments using msDNAs and "Y"-shaped synthetic bRNAs harboring various branchpoint and flanking nucleotides revealed a strong preference for purines at the 2′-flanking nucleotide position and branchpoints flanked by single 2′, 3′, and 5′ nucleotides were sufficient as substrates for yDbr1, suggesting extensive lariat RNA/enzyme interactions are not a prerequisite for branchpoint recognition (22). In subsequent work using comparative sequence analyses, site-directed mutagenesis, and gel-based RNA debranching assays, Khalid et al. concluded that yDbr1 is a manganese-dependent member of the MPE superfamily of enzymes. The addition of exogenous Zn and other divalent cations was found to suppress debranching activity (23).

The first Dbr1 structures determined were from *Entamoeba histolytica* (*Eh*Dbr1) (24). *Eh*Dbr1 is shorter than Dbr1 from higher eukaryotes (354 vs. ∼550 residues) that thus far have been recalcitrant to crystallization. The structures revealed the first 261 residues adopt the canonical MPE fold with adjacent α and β metal-binding pockets. Features unique to Dbr1 include a 28-residue insertion loop immediately adjacent to the active site (residues 130–158) and an invariant cysteine residue (Cys14) in the position of the canonical Asp in the α pocket (25, 26). Because previous work suggested yDbr1 is Mn-dependent (23), 1 mM $MnCl_2$ was added to the EDTA-treated enzyme before crystallization. The resulting wild type and inactive C14S *Eh*Dbr1 structures were unexpectedly mononuclear, with Mn(II) in the β-pocket and a water molecule coordinated to the Mn(II) ion occupying the position expected for the putative α-site metal (26). Alignment of the backbones of structures of *Eh*Dbr1 in complex with product analog 5′-GMP and with a synthetic RNA possessing a 2′-phosphate monoester at the branchpoint adenosine (AK65), superimposed their 5′- and 2′-phosphate moieties, respectively, suggesting a model of an intact lariat branchpoint with flanking nucleotides bound at the active site (24). The conserved 28-residue insertion loop interacts extensively with nucleotides in the putative 3′-arm of the branchpoint and is thus termed the "lariat recognition loop." The data suggested a mononuclear mechanism of hydrolysis in which the invariant α-pocket Cys serves as a catalytic base to activate the metal-bound water nucleophile for attack on the scissile phosphorus atom, with H91 poised to protonate the 2′-O leaving group. However, because essentially all characterized MPEs harbor metal ions in both binding pockets (26) and because Cys residues are excellent ligands for certain metal ions, a binuclear mechanism could not be ruled out (25).

Since the discovery of RNA debranching activity more than 30 years ago, measurement of this activity depended upon gel-based autoradiographic assays in which enzyme and intron lariat substrates are preincubated followed by examination of the mobility of the RNA species postincubation (3, 9, 12, 22, 23, 25). Importantly, however, the metal contents of purified Dbr1 proteins have never been characterized and in the absence of endogenous metal binding information, existing gel-based debranching activity data in which exogenous metal ions were added to purified (and potentially metal-replete) Dbr1 proteins are difficult to interpret (12, 22, 23, 27). More recently, gel-based complementation assays in which Dbr1 and its variants are expressed in *trans* have been developed to probe structure/function relationships via the ability of these proteins to alleviate the intron lariat accumulation phenotype in Δ*dbr1* yeast (23, 25, 28). Although both types of electrophoretic assays are useful as qualitative monitors of debranching activity and as probes of the participation of various amino acid residues in substrate binding and catalysis, they have shed little light upon the kinetic parameters of the enzyme and are complicated by the task of obtaining uniform (and stable) intron lariat substrates.

Here, we measure the kinetics of *Eh*Dbr1-mediated debranching of a fluorogenic bRNA substrate that permits real-time, continuous monitoring of the hydrolysis of 2′,5′-phosphodiester linkages. Inductively coupled plasma mass spectrometry (ICP-MS) analyses reveal that highly active, wild-type *Eh*Dbr1 contains stoichiometric amounts of Ca, Fe, and Zn, but undetectable levels of Mn, Mg, Ni, Co, and Cu. Wild-type *Eh*Dbr1, apo-*Eh*Dbr1 reconstituted with a mixture of Fe and Zn, and apoenzyme reconstituted with Fe(II) hydrolyze the fluorogenic probe at rates between 3–4 s^{-1}. Apo-*Eh*Dbr1 reconstituted with Zn alone yields rates 25–33% slower, whereas apoenzyme reconstituted with Mn alone does not support

debranching activity. Crystal structures of the inactive *Eh*Dbr1 variant H91A in complex with 7-mer and 16-mer bRNAs reveal extensive protein interactions with flanking 2′- and 3′-nucleotides but a paucity of interactions with the 5′-arm. All structures except the apoenzyme are binuclear with a water/hydroxide bridging the Fe and Zn ions in optimal position to attack the scissile phosphate. The results resolve previous uncertainties regarding Dbr1 active site structure and the newly developed dark-quenched bRNA probe is facilitating the screening of large small molecule libraries for Dbr1 inhibitors that may hold promise as therapeutic agents for neurodegenerative diseases such as ALS (29) and for retroviral infections such as HIV (13, 14, 17).

Results

Synthetic bRNAs for Kinetic and Structural Studies. The 10-mer AK88, the 7-mer AK49, and the 16-mer AK86 bRNAs used here were synthesized via solid-phase methods that yield branched oligoribonucleotides of desired length, base composition, and regiochemistry at the branchpoint junction (25) (Fig. 1*B*). The sequence integrity of the synthetic products was cross-validated by using recombinant Dbr1-mediated debranching assays, HPLC, and electrospray ionization mass spectrometry (25, 30). AK88 is designed as a reporter of Dbr1 activity. It possesses a 6-carboxyl-fluorescein (6-FAM) fluorophore covalently linked to the 5′-arm and a 4-([4-(Dimethylamino)phenyl]azo)benzoic acid (DABCYL) quencher covalently linked to the 2′-arm. The proximity of the DABCYL to the 6-FAM suppresses the latter's fluorescence, but this quenching is relieved upon Dbr1-mediated hydrolysis of the 2′,5′-phosphodiester bond (Fig. 1*C*). All three constructs possess the canonical adenosine branchpoint and flanking nucleotides generated when an adenosine nucleotide in the consensus yeast YURAC branch sequence (Y, pyrimidine; R, purine) positioned near the C terminus of the intron acts as the nucleophile to attack the 5′-phosphate of the consensus GU sequence in the donor site positioned at the 5′-end of the intron (Fig. 1*A*, boxed). AK88 was used as a substrate for *Eh*Dbr1 in a continuous fluorometric assay to obtain values of 0.2 ± 0.02 μM for K_m, and 2 ± 0.05 s^{-1} for k_{cat} (Fig. S1). This K_m value agrees with a previous report of a K_d of 0.5 μM for bRNA binding to yDbr1 (31). Electrophoretic analysis of the substrate before and after exposure to Dbr1 indicated that the substrate was completely debranched by Dbr1 (Fig. S2).

Metal Content and Enzymatic Activity. In independent purification runs, wild-type *Eh*Dbr1 expressed in *E. coli* contained, on average, 0.7 eq. Fe, 0.7 eq. Zn, and 1.0 eq. Ca per polypeptide as measured by ICP-MS. Mn, Mg, Ni, Co, Cu, and other divalent cations were undetectable. Addition of Mn, Fe, or Zn to the growth medium did not alter the metal content of the enzyme. Adding exogenous Mn(II) to standard assays did not alter the activity of the purified wild-type enzyme, but the activity of the enzyme decreased in the presence of Zn(II) (Fig. S3). Metal-free *Eh*Dbr1 was prepared by extensive dialysis of freshly purified enzyme against EDTA/NTA-containing buffer (*Materials and Methods* and *SI Materials and Methods*). Reconstitution of the apoenzyme with a mixture of Fe(II) and Zn(II) under aerobic conditions followed by gel filtration to remove excess metal yielded enzyme that catalyzed AK88 hydrolysis at the same rate as the freshly purified holoenzyme, ~3 s^{-1} (Fig. 2*A*). In contrast, apo-Dbr1 reconstituted with Zn(II) alone had a significantly slower rate of less than 1 s^{-1}, and apo-Dbr1 reconstituted aerobically with Mn(II) or Fe(II) alone did not have significant debranching activity (Fig. 2*A*). Of the metals tested (Fe, Zn, Mn), only Fe(II) is sensitive to oxidation by O_2, so the Fe(II) reconstitution was also performed anaerobically. When the apoenzyme was mixed with Fe(II) under anaerobic conditions, the rate exceeded 4 s^{-1} (Fig. 2*A*). The results suggest that Fe(II) added to the apoenzyme under aerobic conditions was oxidized to Fe(III), and that the activity seen with Fe in the β-pocket of the wild-type enzyme (Fig. 3 *A* and *C*) is due to Fe(II).

Crystal Structures of *Eh*Dbr1. The new structures described here include the following: (*i*) wild-type *Eh*Dbr1 containing Fe+Zn (Fig. 3 *A* and *B*); (*ii*) wild-type enzyme stripped of its metal ions (apo-*Eh*Dbr1, Fig. S4); (*iii*) H91A *Eh*Dbr1 in complex with the 7-mer bRNA AK49 (Fig. 3 *C* and *D* and Fig. S5*A*); and (*iv*) H91A *Eh*Dbr1 in complex with the 16-mer bRNA AK86 (Fig. 3*E* and Fig. S6). All *Eh*Dbr1 structures determined to date are isomorphous in space group $P2_12_12_1$ with five protomers in the asymmetric unit. The 20 protomers coming from the four *Eh*Dbr1 structures reported here superimpose with an average rmsd of 0.21 Å for all backbone atoms. Diffraction data and protein structure refinement statistics are given in Table S1. The metal content of H91A *Eh*Dbr1 was similar to that of the wild-type enzyme. The identities of the metal ions in the α and β pockets in the wild-type and AK49/H91A *Eh*Dbr1 complex structures were visualized directly through inspection of anomalous difference Fourier electron density maps by using X-rays tuned to the Fe absorption edge (7.11 keV, 1.74 Å). At this wavelength, iron is illuminated but zinc (9.66 keV, 1.28 Å) is not. The magnitudes of the peaks in the anomalous difference Fourier map reveal that iron partitions predominantly to the β pocket in these structures (Fig. 3 *A* and *C* and Table S2), but Fe is present to varying degrees in the α pocket in the wild-type enzyme (Fig. 3*A* and Table S2). The structures of wild-type *Eh*Dbr1 and H91A *Eh*Dbr1 in complex with AK49 reveal a water/hydroxide bridging the two metal ions, although the positions of the bridging species differ in the RNA-bound versus free forms (compare Fig. 3 *A* and *C*). The Fe ions in the β-sites of both structures are coordinated in a geometry best described as distorted octahedral with D45, N90, H230, and the bridging OH^- serving as equatorial ligands, whereas H180 and either a water molecule (wild-type) or phosphate oxygen atom (AK49 complex) act as axial ligands. In the wild-type enzyme, the α-pocket Zn ion is coordinated in a pseudotrigonal bipyramidal geometry with Cys14, H16, and the bridging OH^- acting as equatorial ligands and D45 and H232 acting as axial ligands. In the AK49 complex, the Zn ion is bound in the α pocket in a distorted octahedral geometry, with H16, D45, H232, and the bridging OH^- serving as equatorial ligands and Cys14 and an oxygen atom coming from the scissile phosphate serving as axial ligands. The distortion in octahedral geometry arises because the scissile phosphate oxygen, the Zn ion, and the S_γ atom of Cys14 are not colinear, with the position of the scissile phosphate oxygen atom displaced from colinearity by ~23° (compare Fig. 3 *B* and *D*). Coordination distances for each of the five protomers in the asymmetric unit are given in Table S2.

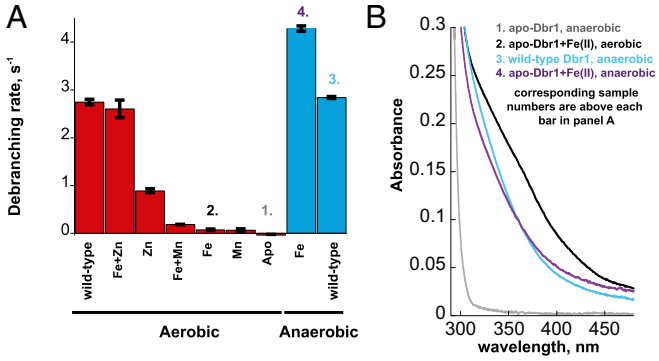

Fig. 2. Effect of added metals on apo-*EhDbr1*. (*A*) The catalytic activity of EhDbr1 with AK88 as substrate was determined after adding the indicated metals to the apoenzyme as described in *Materials and Methods*. The experiments were done aerobically for the samples in red and anaerobically for those in blue. The column labeled wild-type refers to the enzyme before treatment with chelators. (*B*) UV/Vis spectra of selected samples from *A*. The numbering of each trace is shown above its corresponding bar in *A*.

BIOCHEMISTRY

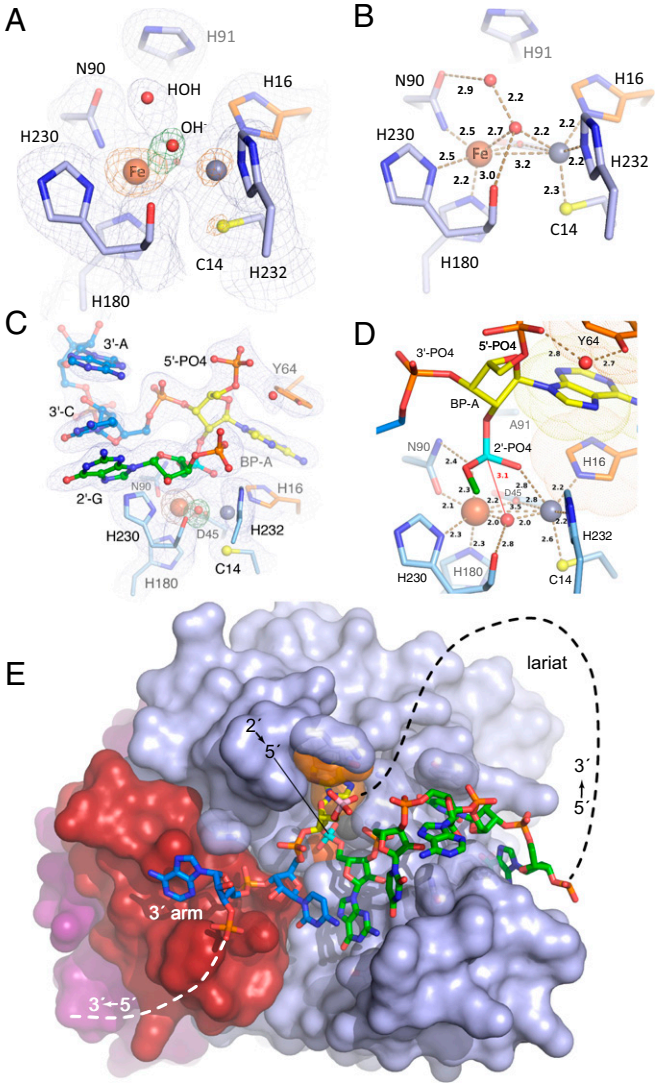

Fig. 3. Structures of wild-type *Eh*Dbr1 alone and its H91A variant in complex with AK49 and AK86. The nucleotide color coding is as in Fig. 1. H16 and Y64 engage in aromatic stacking interactions with the branchpoint adenine and are orange, Fe and Zn ions are rust and gray spheres, respectively, the 2′,5′-linkage is cyan, and the 5′-phosphate of the branchpoint nucleotide is pink. (*A*) σA-weighted $2F_o$-F_c (light blue mesh), F_o-F_c (green mesh), and anomalous difference (orange mesh) electron density maps superimposed on the refined structure of wild-type *Eh*Dbr1 contoured at 1.2, 5.0, and 5.0 σ, respectively. The density for the bridging hydroxide is obscured by the metal ion density in the $2F_o$-F_c map. The F_o-F_c electron density revealing its position was calculated after removing the hydroxide from the refined model. The anomalous difference map was calculated by using X-rays tuned to the Fe absorption edge (see *Results*). (*B*) Coordination distances (Å) for the metal ions in wild-type *Eh*Dbr1. The view is the same as in *A*. (*C*) σA-weighted $2F_o$-F_c, F_o-F_c and anomalous difference electron density maps superimposed on the refined structure of H91A *Eh*Dbr1 in complex with the synthetic 7-mer bRNA AK49 at 1.0, 5.0, and 5.0σ, respectively. (*D*) Coordination distances for the metal ions shown in *C*. For clarity, only the 5′-carbon atom of the flanking 2′-G is shown. (*E*) The 16-mer bRNA AK86 in complex with H91A *Eh*Dbr1. The MPE domain is light blue, the lariat recognition loop is red, and the C-terminal domain is purple. The dashed lines indicate the connectivity in the full intron lariat.

Discussion

A Fluorogenic Assay for Debranching Activity and the Metal Preferences of Dbr1. Until now, characterization of RNA debranching activity depended on gel-based autoradiographic assays in which enzyme and intron lariat substrates were preincubated with millimolar concentrations of $MgCl_2$ (3, 9, 12, 22, 23, 25). Several groups have reported that Dbr1 was required at concentrations 10- to 100-fold over substrate to observe a mobility shift in a reasonable time frame (e.g., 30–60 min). One exception was yDbr1, which acted catalytically in the presence of Mn but not Mg (23). The requirement for a large excess of enzyme in most cases suggests that only a small subset of Dbr1 molecules were active in those assays. The availability of the bRNA substrate AK88 described here permits hydrolysis by purified and reconstituted Dbr1 proteins to be monitored in real time by using a flourometer, thereby providing a simple and convenient way to measure activity.

The data presented here suggest that *Eh*Dbr1 is a binuclear enzyme, with Fe(II) and Zn(II) conferring the highest rates of hydrolysis. First, *Eh*Dbr1 purified after expression in *E. coli* possesses nearly stoichiometric amounts of Fe and Zn, but undetectable levels of Mg, Mn, Co, Ni, Cu, or Cd. Second, the metal centers in the structures of wild-type *Eh*Dbr1 and H91A *Eh*Dbr1 in complex with AK49 reveal binuclear centers with a bridging water molecule/hydroxide ion (Fig. 3 *A*–*D*). Third, *Eh*Dbr1 containing homobinuclear centers Fe(II) or Zn(II) support debranching activities of 4 and 1 s^{-1}, respectively, whereas enzyme containing a heterobinuclear Fe(II)Zn(II) center has a rate of 3 s^{-1} (Fig. 2*A*). Finally, diffraction data from crystals of enzyme using X-rays tuned to the Fe absorption edge reveal that Fe partitions primarily to the β-pocket (Fig. 3 *A* and *C* and Table S2). The observation that metal-free *Eh*Dbr1 reconstituted with a solution of freshly made Fe(II) under aerobic conditions is inactive can be attributed to oxidation to Fe(III), which does not support activity (Fig. 2 *A* and *B*). Taken together, the kinetic and structural data suggest the enzyme requires Fe(II) and/or Zn(II) in the α-pocket for activity.

Yeast Dbr1 was reported to be a manganese-dependent enzyme (23), in contrast to the results reported here with *Eh*Dbr1. Thus, available evidence indicates that yDbr1 and EhDbr1 have different metal cofactor requirements. We cannot rule out the possibility that *Eh*Dbr1 is active with Mn, but the affinity of that metal for the enzyme is much lower than the affinity for Fe or Zn (Fe was not tested with the yeast enzyme). We have found that *Eh*Dbr1 precipitates in the presence of mM Zn; this precipitation may explain the lack of observed activity of the yeast enzyme in the presence of 2.5 mM Zn. The lack of an effect of added Mn on wild-type *Eh*Dbr1 (Fig. S3) can be attributed to that enzyme already having a full complement of metal bound.

Mechanism of Dbr1-Mediated Intron Debranching. The structure of the Fe+Zn-containing wild-type enzyme represents the resting state (Fig. 3 *A* and *B*), whereas the structure of the *Eh*Dbr1 variant H91A in complex with AK49 represents a snapshot of the bRNA/enzyme complex immediately before hydrolysis. Our previous structural work on mononuclear *Eh*Dbr1 implicated H91 as the catalytic acid (24) because it appears poised to protonate the 2′-O leaving group during hydrolysis in the structure of the *Eh*Dbr1/AK65 complex. Indeed, H91A *Eh*Dbr1 is inactive, enabling the first direct visualizations of bona fide 2′,5′-phosphodiester linkages bound to the enzyme. The position of the bridging water/hydroxide in the resting state (Fig. 3 *A* and *B*) is approximately the same as the scissile phosphorous atom of the 2′,5′-phosphodiester linkage in the *Eh*Dbr1/AK49 complex (Fig. 3 *C* and *D*). Upon binding of AK49, the bridging aquo species is displaced to a new bridging position where it is stabilized by a hydrogen bond to the carbonyl oxygen of H230, a ligand to the β-pocket Fe atom (Fig. 3 *C* and *D*). The active site structure suggests a S_N2 mechanism of hydrolysis in which the metal ions serve as Lewis acids to polarize the bridging oxygen-phosphorous bonds, increasing the electrophilic character of the scissile phosphorous (Fig. 4). The position of the bridging OH^- species appears optimal for nucleophilic attack at a distance of 3.1 Å. The reaction is predicted to proceed through a trigonal bipyramidal pentacoordinate transition state with inversion of configuration and protonation of the 2′-O leaving

group by H91. The proposed flow of electrons during catalysis is shown in Fig. 4.

Dbr1/bRNA Interactions. The structures of the 7-mer and 16-mer bRNAs AK49 and AK86 in complex with the *Eh*Dbr1 variant H91A provide insight into the molecular basis for bRNA recognition. AK49 possesses two nucleotides in its 2′-, 3′-, and 5′-arms, whereas AK86 possesses five nucleotides in each arm. The branchpoint and flanking nucleotides of both constructs mimic those found in the *S. cerevisiae* consensus splice site (Fig. 1 *A* and *B*). The 5′-arms are disordered in both structures, suggesting they do not play a significant role in branchpoint recognition. In contrast, extensive enzyme/bRNA interactions occur at the branchpoint adenosine, the flanking guanosine in the 2′-arm and the flanking cytidine and adenosine of the 3′-arm. Together, these four nucleotides participate in eight protein/RNA hydrogen bonds, three protein/RNA aromatic stacking interactions, and one RNA/RNA base stacking interaction (Fig. S5*A*). The flanking 2′-G forms hydrogen bonds with the side chains of G101 and D205 and base stacks with the cytidine of the flanking 3′-C that, in turn, donates two hydrogen bonds to the side chain of K134 of the lariat recognition loop (LRL). LRL residues I132, F155, and H156 make extensive contacts with the ribose ring and the 3′-,5′-phosphodiester bond linking the 3′-C and terminal 3′-A (Fig. S5*A*). The second flanking nucleotide in the 3′-arm (3′-A) base-stacks with the side chain of F136 of the LRL. Although two nucleotides are present in the 2′-arm of AK49, only the flanking guanosine is visible in the structure of the complex (Fig. S5*A*). The extent of these interactions is consistent with previous findings that a trinucleotide consisting of a branchpoint adenosine with single flanking 2′- and 3′-nucleotides is recognized and cleaved by Dbr1 (12).

In contrast, in the structure of the AK86/*Eh*Dbr1 complex, all five nucleotides of the 2′-arm are visible and these nucleotides engage the enzyme at the junction of a β-hairpin formed by residues 233–249 and a helix-turn-helix insertion element formed by residues 179–212 (Fig. S6). Together, these structural elements form a platform that projects from the metal center around which the nucleotides of the 2′-arm wrap. The third nucleotide of the 2′-arm (adenosine) is completely devoid of interactions with protein (Fig. 3*E* and Fig. S6). The fourth and fifth nucleotides in the 2′-arm make aromatic stacking interactions with Y252 and F198, respectively. The aromatic base-stacking between the flanking 2′-G, and 3′-C (Fig. 3*E* and Figs. S5 and S6) combined with extensive interactions with the enzyme cause the branchpoint adenine base to be exposed and to protrude in a direction opposite to the flanking stacking 2′- and 3′-bases, where it is sandwiched in aromatic stacking interactions between H16 and Y64. In their seminal 1985 paper, Ruskin and Green (3) reported poly-A RNA linked solely by 2′,5′-phosphodiester bonds is not a substrate for human Dbr1. The structure of the AK49/*Eh*Dbr1 complex permits rationalization of this observation. If 2′,5′-linked poly-A RNA binds analogously to the branchpoint adenosine in AK49 and AK86, the 2′-G is replaced by a 2′-A with the loss of two protein–RNA hydrogen-bonding interactions (Fig. S5*B*). Because 2′,5′-linked poly-A RNA does not possess the equivalent of a 3′-arm, it would be devoid of all of the previously stabilizing interactions. In addition, the 5′,3′-phosphodiester bond linking the 2′-G and 2′-U in AK86 and AK49 (Fig. 3*E* and Fig. S5*A*) would be replaced by a 2′,5′-phosphodiester linkage between adenosine nucleotides, a linkage predicted to clash with F202 and other nearby residues (Fig. S5*B*).

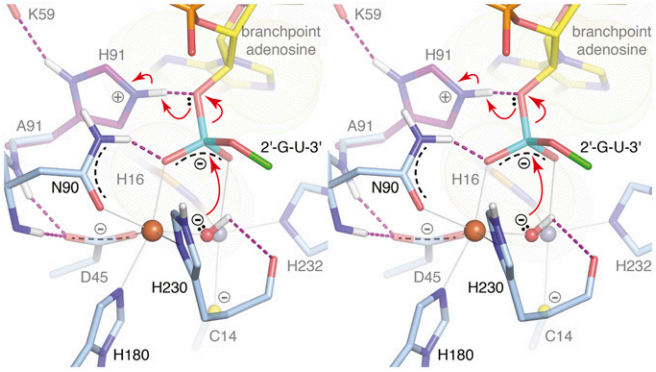

Fig. 4. Divergent stereoview of the proposed mechanism of *Eh*Dbr1-mediated hydrolysis of intron lariats. The bridging OH^- is in position for nucleophilic attack on the 2′, 5′-phosphodiester linkage. The reaction proceeds via a S_N2 mechanism of hydrolysis through a trigonal bipyramidal pentacoordinate intermediate, followed by inversion of configuration and concludes when the 2′-O leaving group is protonated by H91. The red arrows indicate electron flow during the reaction.

The Invariant Cys in the α-Pocket of Dbr1 Enzymes. MPEs possess the conserved signature sequence $\underline{D}_{\alpha}$[X]$\underline{H}_{\alpha}$ [X]$_n$ G$\underline{D}_{\alpha+\beta}$ [X]$_n$ G$\underline{N}_{\beta}$H[D/E] [X]$_n$ $\underline{H}_{\beta}$ [X]$_n$ G$\underline{H}_{\alpha}$[X]$\underline{H}_{\beta}$, where underlined/italicized letters correspond to metal ligands, α and β to the binding pockets in which the ligands reside, and X to any amino acid (26). Despite the conservation of metal-binding residues, the repertoire used by various MPEs is diverse and signature sequence-containing enzymes bind Mn(II), Fe(II), Fe(III), Zn(II), Co(II), Cd(II), and Ni(II) (reviewed in ref. 26). Normally, Fe(II) and Mn(II) tend to prefer similar coordination environments, making it difficult for some proteins to distinguish between them on the basis of active site structures alone (32). Indeed, the insertion of the "correct" metal ion into a metalloprotein often depends on the relative concentrations of various metal ions in the immediate environment during and after protein folding as well as the affinity and selectivity of the nascent (apo) metalloprotein for its metal cofactor (reviewed in ref. 32). Fe(II) and Zn(II) are abundant in biological systems, at levels ∼50-fold higher than Mn(II) [∼300 μM vs. 6 μM; ref. 33). Still, Mn(II) is commonly found in MPEs and was reported to support the highest phosphoesterase activity among divalent cations tested in Mre11 (34, 35), 5′-nucleotidase (36, 37), MPPED2 (38, 39), and yeast Dbr1 (23). Superposition of the Mre11 and Dbr1 binuclear centers reveals they are indeed similar, including the position of the bridging nucleophile, except for the substitution of the first aspartic acid in the signature sequence with Cys in Dbr1 (Fig. S7). Examples of Cys serving as a ligand to Mn(II) are rare, with the RNA ligase RtcB being a notable example (40). In the MESPEUS database of metal sites in proteins (mined from the PDB), there are 35 examples of Cys coordinating Mn ions, 6,023 examples of Cys coordinating Fe ions, and 8,069 examples of Cys coordinating Zn ions (41). The inability of the α-pocket of Dbr1 to bind Mn(II) was evident in previous work in which EDTA-treated *Eh*Dbr1 crystallized in the presence of 1 mM $MnSO_4$ with Mn(II) only in the β-pocket (24). Even when the concentration of $MnSO_4$ in the crystallization buffer was increased to 10 mM, there was no Mn in the α-pocket.

We speculate that the presence of the α-pocket Cys ligand reflects the metal preferences of Dbr1. Although Fe(II) and Zn(II) provide the highest turnover rates in our kinetic assays with *Eh*Dbr1 (Fig. 2), it remains to be demonstrated that other Dbr1 orthologs (such as yeast Dbr1) also prefer Fe(II) and Zn(II). More experiments are required to explain why Dbr1 enzymes harbor a Cys in the α-pocket, instead of the Asp found in other MPEs. Whether modulation of Fe(II) and Zn(II) levels affects Dbr1 activity in vivo also remains to be demonstrated.

Materials and Methods

Detailed procedures are given in *SI Materials and Methods*. Briefly, the *DBR1* gene from *E. histolytica* was codon optimized (DNA 2.0; Genescript), expressed as a His-tagged fusion protein in *E. coli* strain BL21 (New England Biolabs), and purified by using a Ni-Sepharose Fast Flow column (GE Healthcare). The metal

BIOCHEMISTRY

content was determined by ICP-MS at the Chemical Analysis Laboratory at the University of Georgia. Apoenzyme was obtained by dialyzing Dbr1-containing fractions against stripping buffer [10 mM EDTA, 10 mM NTA, 20 mM Hepes pH 7, 50 mM NaCl, and 1 mM tris(2-carboxyethyl)phosphine (TCEP)] at 4 °C for 72 h followed by dialysis against assay buffer (50 mM Hepes pH 7, 100 mM NaCl) that had been treated with 10 g of Chelex resin (Bio-Rad) per liter of buffer. Kinetic assays were performed by using 5 μM enzyme (final concentration) to eliminate effects of trace metal ions remaining in the assay buffer. A Pherastar plate reader (BMG Labtech) in rapid kinetic mode and a stopped-flow mixing spectrophotometer (Applied Photophysics) were used for aerobic and anaerobic kinetic assays, respectively. For measurement of steady-state kinetic parameters, the inner-filter effect was corrected for using the method described in ref. 42. Crystals of *Eh*Dbr1 grew in 0.1 M Bis-Tris pH 5.5 made 10–17% (wt/vol) PEG 3350, 0.4 M $LiSO_4$, 10% (vol/vol) glycerol in hanging-drop plates. Diffraction data were taken at the Advanced Photon Source 24 ID-C beamline with a Pilatus-6MF Pixel Array Detector operated by Northeast Collaborative Access Team (NE-CAT). The programs XDS (43), AIMLESS (44), PHENIX (45), and COOT (46) were used for data integration, scaling, model refinement, and model building, respectively. Structure factors and model coordinates are deposited in the PDB with codes: 5K71, 5K73, 5K77, and 5K78 for apo-, wild-type, AK49/H91A, and AK86/H91A Dbr1 structures, respectively.

ACKNOWLEDGMENTS. P.J.H. was supported in part by Merit Review Award I01 BX0025801 from the US Department of Veterans Affairs, Biomedical Laboratory Research and Development Service, S. Texas Veterans Health Care System, and in part by a Welch Foundation Grant AQ-1399 and by the Judith and Jean Pape Adams Charitable Foundation. M.J.D. was supported by a Discovery Grant from the National Sciences and Engineering Research Council of Canada. S.W.S. was supported by National Institutes of Health (NIH) Grant GM084246. N.E.C. and E.J.M. were supported by NIH Grant T-32 AG021890 through the Barshop Institute for Longevity and Aging Studies. E.J.M. was supported by Grant DBI-0905865 through the National Science Foundation. P.F.F. and K.M.R. were supported by Grant AQ-1245 from The Welch Foundation. Support for NE-CAT beamline 24-ID-E is provided by NIH Grant P41 GM103403 and US Department of Energy Grant DE–AC02–06CH11357. The X-Ray Core Laboratory at University of Texas Health Science Center, San Antonio (UTHSCSA) is supported in part by the Office of the Vice President for Research and by San Antonio Cancer Institute Grant P30 CA054174. Equipment and technical expertise were provided by the Center for Innovative Drug Discovery and High Throughput Screening Facility at UTHSCSA, which is supported by Grant UL1 TR001120 from the National Center for Advancing Translational Sciences, NIH.

1. Moore MJ, Sharp PA (1993) Evidence for two active sites in the spliceosome provided by stereochemistry of pre-mRNA splicing. *Nature* 365(6444):364–368.
2. Konarska MM, Grabowski PJ, Padgett RA, Sharp PA (1985) Characterization of the branch site in lariat RNAs produced by splicing of mRNA precursors. *Nature* 313(6003): 552–557.
3. Ruskin B, Green MR (1985) An RNA processing activity that debranches RNA lariats. *Science* 229(4709):135–140.
4. Okamura K, Hagen JW, Duan H, Tyler DM, Lai EC (2007) The mirtron pathway generates microRNA-class regulatory RNAs in Drosophila. *Cell* 130(1):89–100.
5. Ooi SL, Samarsky DA, Fournier MJ, Boeke JD (1998) Intronic snoRNA biosynthesis in Saccharomyces cerevisiae depends on the lariat-debranching enzyme: Intron length effects and activity of a precursor snoRNA. *RNA* 4(9):1096–1110.
6. Domdey H, et al. (1984) Lariat structures are in vivo intermediates in yeast pre-mRNA splicing. *Cell* 39(3 Pt 2):611–621.
7. Matera AG, Wang Z (2014) A day in the life of the spliceosome. *Nat Rev Mol Cell Biol* 15(2):108–121.
8. Chapman KB, Boeke JD (1991) Isolation and characterization of the gene encoding yeast debranching enzyme. *Cell* 65(3):483–492.
9. Nam K, Lee G, Trambley J, Devine SE, Boeke JD (1997) Severe growth defect in a Schizosaccharomyces pombe mutant defective in intron lariat degradation. *Mol Cell Biol* 17(2):809–818.
10. Wang H, Hill K, Perry SE (2004) An Arabidopsis RNA lariat debranching enzyme is essential for embryogenesis. *J Biol Chem* 279(2):1468–1473.
11. Zheng S, et al. (2015) Non-coding RNA generated following lariat debranching mediates targeting of AID to DNA. *Cell* 161(4):762–773.
12. Arenas J, Hurwitz J (1987) Purification of a RNA debranching activity from HeLa cells. *J Biol Chem* 262(9):4274–4279.
13. Galvis AE, Fisher HE, Nitta T, Fan H, Camerini D (2014) Impairment of HIV-1 cDNA synthesis by DBR1 knockdown. *J Virol* 88(12):7054–7069.
14. Ye Y, De Leon J, Yokoyama N, Naidu Y, Camerini D (2005) DBR1 siRNA inhibition of HIV-1 replication. *Retrovirology* 2:63.
15. Deininger PL, Batzer MA (2002) Mammalian retroelements. *Genome Res* 12(10): 1455–1465.
16. Koonin EV (2006) The origin of introns and their role in eukaryogenesis: A compromise solution to the introns-early versus introns-late debate? *Biol Direct* 1:22.
17. Cheng Z, Menees TM (2004) RNA branching and debranching in the yeast retrovirus-like element Ty1. *Science* 303(5655):240–243.
18. Cheng Z, Menees TM (2011) RNA splicing and debranching viewed through analysis of RNA lariats. *Mol Genet Genomics* 286(5-6):395–410.
19. Salem LA, Boucher CL, Menees TM (2003) Relationship between RNA lariat debranching and Ty1 element retrotransposition. *J Virol* 77(23):12795–12806.
20. Coombes CE, Boeke JD (2005) An evaluation of detection methods for large lariat RNAs. *RNA* 11(3):323–331.
21. Ooi SL, et al. (2001) RNA lariat debranching enzyme. *Methods Enzymol* 342:233–248.
22. Nam K, et al. (1994) Yeast lariat debranching enzyme. Substrate and sequence specificity. *J Biol Chem* 269(32):20613–20621.
23. Khalid MF, Damha MJ, Shuman S, Schwer B (2005) Structure-function analysis of yeast RNA debranching enzyme (Dbr1), a manganese-dependent phosphodiesterase. *Nucleic Acids Res* 33(19):6349–6360.
24. Montemayor EJ, et al. (2014) Structural basis of lariat RNA recognition by the intron debranching enzyme Dbr1. *Nucleic Acids Res* 42(16):10845–10855.
25. Katolik A, et al. (2014) Regiospecific solid-phase synthesis of branched oligoribonucleotides that mimic intronic lariat RNA intermediates. *J Org Chem* 79(3):963–975.
26. Matange N, Podobnik M, Visweswariah SS (2015) Metallophosphoesterases: Structural fidelity with functional promiscuity. *Biochem J* 467(2):201–216.
27. Ruskin B, Green MR (1990) RNA lariat debranching enzyme as tool for analyzing RNA structure. *Methods Enzymol* 181:180–188.
28. Kim JW, et al. (2000) Human RNA lariat debranching enzyme cDNA complements the phenotypes of Saccharomyces cerevisiae dbr1 and Schizosaccharomyces pombe dbr1 mutants. *Nucleic Acids Res* 28(18):3666–3673.
29. Armakola M, Hart MP, Gitler AD (2011) TDP-43 toxicity in yeast. *Methods* 53(3): 238–245.
30. Tago N, et al. (2015) Design, synthesis, and properties of Phosphoramidate 2′,5′-linked branched RNA: Toward the rational design of inhibitors of the RNA lariat debranching enzyme. *J Org Chem* 80(20):10108–10118.
31. Garrey SM, et al. (2014) A homolog of lariat-debranching enzyme modulates turnover of branched RNA. *RNA* 20(8):1337–1348.
32. Cotruvo JA, Jr, Stubbe J (2012) Metallation and mismetallation of iron and manganese proteins in vitro and in vivo: The class I ribonucleotide reductases as a case study. *Metallomics* 4(10):1020–1036.
33. Cunzhi H, et al. (2003) Serum and tissue levels of six trace elements and copper/zinc ratio in patients with cervical cancer and uterine myoma. *Biol Trace Elem Res* 94(2):113–122.
34. Hopfner KP, et al. (2001) Structural biochemistry and interaction architecture of the DNA double-strand break repair Mre11 nuclease and Rad50-ATPase. *Cell* 105(4): 473–485.
35. Hopfner KP, et al. (2000) Mre11 and Rad50 from Pyrococcus furiosus: Cloning and biochemical characterization reveal an evolutionarily conserved multiprotein machine. *J Bacteriol* 182(21):6036–6041.
36. Knöfel T, Sträter N (2001) Mechanism of hydrolysis of phosphate esters by the dimetal center of 5′-nucleotidase based on crystal structures. *J Mol Biol* 309(1):239–254.
37. McMillen L, Beacham IR, Burns DM (2003) Cobalt activation of Escherichia coli 5′-nucleotidase is due to zinc ion displacement at only one of two metal-ion-binding sites. *Biochem J* 372(Pt 2):625–630.
38. Dermol U, Janardan V, Tyagi R, Visweswariah SS, Podobnik M (2011) Unique utilization of a phosphoprotein phosphatase fold by a mammalian phosphodiesterase associated with WAGR syndrome. *J Mol Biol* 412(3):481–494.
39. Tyagi R, Shenoy AR, Visweswariah SS (2009) Characterization of an evolutionarily conserved metallophosphoesterase that is expressed in the fetal brain and associated with the WAGR syndrome. *J Biol Chem* 284(8):5217–5228.
40. Desai KK, Bingman CA, Phillips GN, Jr, Raines RT (2013) Structures of the noncanonical RNA ligase RtcB reveal the mechanism of histidine guanylylation. *Biochemistry* 52(15): 2518–2525.
41. Hsin K, Sheng Y, Harding MM, Taylor P, Walkinshaw MD (2008) MESPEUS: A database of the geometry of metal sites in proteins. *J Appl Cryst* 41:963–968.
42. Liu Y, et al. (1999) Use of a fluorescence plate reader for measuring kinetic parameters with inner filter effect correction. *Anal Biochem* 267(2):331–335.
43. Kabsch W (2010) Xds. *Acta Crystallogr D Biol Crystallogr* 66(Pt 2):125–132.
44. Evans PR, Murshudov GN (2013) How good are my data and what is the resolution? *Acta Crystallogr D Biol Crystallogr* 69(Pt 7):1204–1214.
45. Adams PD, et al. (2010) PHENIX: A comprehensive Python-based system for macromolecular structure solution. *Acta Crystallogr D Biol Crystallogr* 66(Pt 2):213–221.
46. Emsley P, Lohkamp B, Scott WG, Cowtan K (2010) Features and development of Coot. *Acta Crystallogr D Biol Crystallogr* 66(Pt 4):486–501.
47. Roberts KM, Pavon JA, Fitzpatrick PF (2013) Kinetic mechanism of phenylalanine hydroxylase: Intrinsic binding and rate constants from single-turnover experiments. *Biochemistry* 52(6):1062–1073.
48. Ellis HR, McCusker KP, Fitzpatrick PF (2002) Use of a tyrosine hydroxylase mutant enzyme with reduced metal affinity allows detection of activity with cobalt in place of iron. *Arch Biochem Biophys* 408(2):305–307.
49. Keating KS, Pyle AM (2010) Semiautomated model building for RNA crystallography using a directed rotameric approach. *Proc Natl Acad Sci USA* 107(18):8177–8182.